https://doi.org/10.5194/egusphere-2024-3460
Preprint. Discussion started: 2 January 2025

Decomposition of three aerosol components using lidar-derived depolarization ratios at two wavelengths

Xiaoxia Shang[1], Maria Filioglou[1], Julian Hofer[2], Moritz Haarig[2], Qiaoyun Hu[3], Philippe Goloub[3], Sami Romakkaniemi[1], and Mika Komppula[1]

[1]Finnish Meteorological Institute, Kuopio, Finland.
[2]Leibniz Institute for Tropospheric Research, Leipzig, Germany
[3]Univ. Lille, CNRS, UMR 8518 – LOA – Laboratoire d'Optique Atmosphérique, 59000 Lille, France

Correspondence: Xiaoxia Shang (xiaoxia.shang@fmi.fi)

Abstract. In this study, we present a novel algorithm using the lidar-derived particle linear depolarization ratios measured at two wavelengths for the decomposition of three aerosol components, to retrieve aerosol-type-specific backscatter fractions. This extended methodology builds upon well-developed polarization-based algorithms, e.g., POLIPHON (POlarization LIdar PHOtometer Networking) method, offers an added advantage for an almost unambiguous separation of three aerosol components, on the condition that their characteristic depolarization ratios are different. And it requires the proper knowledge of characteristic depolarization ratio and the backscatter-related Ångström exponent of each aerosol type. The mathematical relationship between particle linear depolarization ratios at two wavelengths for a mixture of two aerosol components has been derived and expressed as an equation. This equation is visualized as a curved line, where the boundaries are determined by the characteristic depolarization ratios and the curvature is influenced by the characteristic backscatter-related Ångström exponents of both aerosol types. Moreover, the pair values of particle linear depolarization ratios of three aerosol components at two wavelengths must remain within the enclosed region predetermined by three boundary curves, and each curve is determined by the characteristics of any two of three types. Such characteristic curved relationships are more accurate than the common use of the ratio of the particle linear depolarization ratios. This novel algorithm has been applied to synthetic examples considering dust mixtures and to lidar observations of Arabian dust, Asian dust, and Saharan dust, so as to decompose coarse-mode dust (>1 μm in diameter), fine-mode dust (<1 μm in diameter), and spherical non-dust aerosols. The dust characteristics reported in numerous laboratory and field studies have been considered.

1 Introduction

Light detection and ranging (lidar) is a powerful instrument that provides vertical information of atmospheric aerosol and clouds from ground and space at high vertical resolution. Irregularly shaped particles induce strong depolarization of laser light. Polarization-based algorithms have been developed to separate the aerosol profiles of weakly light depolarizing (spherical, e.g., anthropogenic haze, biomass burning smoke, maritime) and strongly light depolarizing (non-spherical, e.g., volcanic ash, desert dust, pollen) particles (e.g., Shimizu et al., 2004; Tesche et al., 2009, 2011; Ansmann et al., 2011, 2012; Sugimoto and Lee, 2006; Nishizawa et al., 2007; Freudenthaler et al., 2009; Groß et al., 2011, 2012; Miffre et al., 2012; Nisantzi et al.,

https://doi.org/10.5194/egusphere-2024-3460
Preprint. Discussion started: 2 January 2025

2014; Shang et al., 2020). Such techniques have been primarily used for decoupling the particle backscatter coefficient profiles of, e.g., dust and non-dust particles (Tesche et al., 2009), ash and fine-mode particles (Ansmann et al., 2011; Marenco and Hogan, 2011), and pollen and non-depolarizing background aerosol (Shang et al., 2022). In addition, the POLIPHON (POlarization LIdar PHOtometer Networking) method (Ansmann et al., 2012) allows the retrieval of the particle number, surface area, and volume/mass concentration of fine mode and coarse mode particles, in synergy with sun-sky photometer measurements (one-step POLIPHON). The extended POLIPHON method, namely the two-step POLIPHON method, further allows the separation of non-dust, fine mode, and coarse mode dust particle contributions of the above-mentioned optical and microphysical quantities (Mamouri and Ansmann, 2014, 2017). The two-step POLIPHON method comprises two subsequent phases similar to the one-step POLIPHON, and allows separating three aerosol components, as long as their characteristic depolarization ratios are distinct. However, to separate the backscatter coefficients of coarse mode dust in the first step, it requires an assumption about the spherical particle fraction to estimate the overall depolarization ratio for the residual aerosol (a mixture of non-dust and fine-dust with unknown mixing ratio). To date, POLIPHON has been utilized in many studies, to lidar observations exploiting single-wavelength polarization measurements (Ansmann et al., 2019; Córdoba-Jabonero et al., 2018; Mamali et al., 2018; Haarig et al., 2019; Proestakis et al., 2024).

Most commonly, the 532 nm and 355 nm wavelengths have been used to perform depolarization ratio measurements. Most lidar stations in the European Aerosol Research Lidar Network (EARLINET, Pappalardo et al. (2014); https://www.earlinet.org, last access: 10 October 2024) and the Raman and polarization lidar network (PollyNET, Baars et al. (2016); https://polly.tropos.de, last access: 10 October 2024) measure the particle linear depolarization ratios at 532 and/or 355 nm. The NASA Micro-Pulse Lidar Network (MPLNET, Welton et al. (2001); https://mplnet.gsfc.nasa.gov, last access: 10 October 2024) provide polarization measurements at 532 nm. The space-borne lidars CALIOP (Cloud-Aerosol LIdar with Orthogonal Polarization) onboard the CALIPSO (the Cloud-Aerosol Lidar and Infrared Pathfinder Satellite Observation) (Winker et al., 2009), and ATLID (Atmospheric Lidar) in the ESA's EarthCARE (Cloud, Aerosol and Radiation Explorer; https://earth.esa.int/eogateway/missions/earthcare, last access: 10 October 2024) mission retrieve depolarization ratio at 532 or 355 nm, respectively. Depolarization ratio observations at 1064 nm have been increasing the last years as well (Haarig et al., 2022; Hu et al., 2020). The Vaisala CL61 ceilometer, and the HALO Photonics Stream Line Pro scanning Doppler lidar (Pearson et al., 2009) also provide polarization observations at 910 nm and 1565 nm, respectively. The utilization of the multi-wavelength polarization lidar or a synergy of multiple lidars with the capability to provide concurrent depolarization ratio observations at various wavelengths allows the investigation of the spectral dependence on the depolarization ratios. This is an important aspect to characterize different aerosol types, such as dust (Haarig et al., 2017a, 2022) and pollen (Bohlmann et al., 2021; Filioglou et al., 2023). In particular, it could enable the distinction of non-spherical aerosol types.

In this study, we present a novel methodology (Sect. 2), using the particle linear depolarization ratios measured at two wavelengths, to separate the particle backscatter coefficients of three aerosol components without introducing assumptions regarding the aerosol particle fractions as required in the POLIPHON method. The relationship between particle linear depolarization ratios at two wavelengths are investigated mathematically for mixtures of two and three aerosol components. Then, the method is applied to lidar observations of dust particles at different regions (Sect. 3).

https://doi.org/10.5194/egusphere-2024-3460
Preprint. Discussion started: 2 January 2025

2 Methodology

The particle linear depolarization ratio of the particle ensemble at wavelength λ, denoted as $\delta_p(\lambda)$, can be expressed by Eqs. 1–2 for an aerosol mixture of two or three externally mixed aerosol types (Shimizu et al., 2004; Tesche et al., 2009; Mamouri and Ansmann, 2014). In this context, each particle consists of a single aerosol type, and the calculation involves the aerosol backscatter coefficient (β_x) and aerosol-type-specific characteristic depolarization ratio (δ_x), where the index x corresponds to each aerosol type (a, or b, or c).

$$\delta_p(\lambda) = \frac{\frac{\beta_a(\lambda)\delta_a(\lambda)}{\delta_a(\lambda)+1} + \frac{\beta_b(\lambda)\delta_b(\lambda)}{\delta_b(\lambda)+1}}{\frac{\beta_a(\lambda)}{\delta_a(\lambda)+1} + \frac{\beta_b(\lambda)}{\delta_b(\lambda)+1}} \quad (1)$$

$$\delta_p(\lambda) = \frac{\frac{\beta_a(\lambda)\delta_a(\lambda)}{\delta_a(\lambda)+1} + \frac{\beta_b(\lambda)\delta_b(\lambda)}{\delta_b(\lambda)+1} + \frac{\beta_c(\lambda)\delta_c(\lambda)}{\delta_c(\lambda)+1}}{\frac{\beta_a(\lambda)}{\delta_a(\lambda)+1} + \frac{\beta_b(\lambda)}{\delta_b(\lambda)+1} + \frac{\beta_c(\lambda)}{\delta_c(\lambda)+1}} \quad (2)$$

The aerosol backscatter fraction ϕ_x (Eq. 3) is defined as the ratio of the backscatter coefficient of the aerosol type x (β_x) to the total particle backscatter coefficient (β_p). The sum of all aerosol backscatter fractions in the particle ensemble is equal to 1.

$$\phi_x(\lambda) = \frac{\beta_x(\lambda)}{\beta_p(\lambda)} \quad (3)$$

The backscatter-related Ångström exponent (Å_β) between two wavelengths, λ_1 and λ_2, can be expressed through Eq. 4 (the index x can be used for one aerosol type or for the particle ensemble), where parameter η, often refereed as the backscatter color ratio, is a function of Å_β and it is defined as follows:

$$\eta_x = (\frac{\lambda_1}{\lambda_2})^{-\text{Å}_{\beta,x}(\lambda_1,\lambda_2)} = \frac{\beta_x(\lambda_1)}{\beta_x(\lambda_2)}. \quad (4)$$

To apply the novel algorithm for the decomposition of two or three aerosol components, proper knowledge of the characteristic depolarization ratios (δ_x) and backscatter-related Ångström exponent ($\text{Å}_{\beta,x}$) of each aerosol type is necessary. The fine and coarse mode dust optical properties have been measured and reported in many laboratory and field studies (Sakai et al., 2010; Järvinen et al., 2016; Freudenthaler et al., 2009; Burton et al., 2015). Due to the distinct depolarization ratios of fine and coarse mode dust, and spherical non-dust aerosols, these aerosols become good candidates for validating the novel methodology. Atmospheric mineral dust is one of the most important aerosol types, playing a key role on several critical aspects of the Earth system. As stated in Adebiyi et al. (2023), Castellanos et al. (2024), and references therein, many studies have been performed to investigate the dust properties. The size of mineral dust in the atmosphere ranges from less than 0.1 μm to more than 100 μm in diameter (Adebiyi et al., 2023; Ryder et al., 2019; van der Does et al., 2018; Mahowald et al., 2014). Following the POLIPHON method, in this study, we consider two components of pure dust: fine-mode dust which covers the particle size spectrum up to 1 μm in diameter, and coarse-mode dust with super-micrometer particles (>1 μm in diameter).

https://doi.org/10.5194/egusphere-2024-3460
Preprint. Discussion started: 2 January 2025

The algorithm was applied to synthetic examples considering dust mixture in Sect. 2, and to lidar observations of dust at different regions in Sect. 3, using the characteristics from Table 1. The characteristic depolarization ratios of coarse and fine mode dust at 355, 532, and 1064 nm are taken from the review study of Mamouri and Ansmann (2017) (see Table 1 in that paper), which includes two laboratory studies (Sakai et al., 2010; Järvinen et al., 2016), and five field observations (Freudenthaler et al., 2009; Burton et al., 2015; Veselovskii et al., 2016; Haarig et al., 2017a; Hofer et al., 2017). The laboratory experiments to measure the airborne dust properties is challenging, and thus still limit. Sakai et al. (2010) measured $\delta_x(532)$ of several tropospheric aerosols using a laboratory chamber. For high number concentrations, $\delta_{df}(532)$ of the fine-mode dust were found to be 0.17 ± 0.03 for the Asian dust and 0.14 ± 0.03 for the Saharan dust, whereas $\delta_{dc}(532)$ of the coarse-mode dust were 0.39 ± 0.04 to 0.05 for both. Järvinen et al. (2016) measured δ_{dust} of various dust samples at 488 and 552 nm in a cloud chamber. They reported that the measured δ_{dust} ranged from 0.03 to 0.36 and were strongly dependent on the particle size. Based on this study, Mamouri and Ansmann (2017) estimated δ_{df} for fine-mode dust of around 0.21 ± 0.02, 0.16 ± 0.02, and 0.09 ± 0.03 for the laser wavelengths of 355, 532, and 1064 nm, respectively. Miffre et al. (2023) found that the dust depolarization ratios are mainly influenced by the particles' complex refractive index, when the strongly light-absorbing hematite is present, while its variations with size and shape are less significant. They also present measured δ_{dust} values for finer and coarser size distributions of Arizona and Asian dust (see Table 1 in Miffre et al., 2023), which can not be used in this study as the used size distributions are different from other studies. Field measurements were also considered. Nevertheless, the reported characteristic depolarization ratios from field observations may still contain contributions from spherical particles within the mixture, potentially leading to an underestimation of the characteristic values. Moreover, certain vertical smoothing is always applied in the lidar retrievals, and layer-mean values are often reported, adding uncertainties on the lidar-derived characteristics of aerosol types. Burton et al. (2015) performed airborne measurements of dust plumes over the United States. For a dense dust layer of local North American dust, they found high δ_p of 0.24 ± 0.05, 0.37 ± 0.01, 0.38 ± 0.01 at 355, 532, and 1064 nm, respectively. The corresponding $\mathring{A}_\beta(532, 1064)$ is -0.09 ± 0.04. For two transported Saharan dust layers, $\mathring{A}_\beta(532, 1064)$ were found to be 0.46 ± 0.03 and 0.68 ± 0.13. Veselovskii et al. (2016) observed that $\delta_p(532)$ increased up to 0.35 ± 0.05, and $\mathring{A}_\beta(355, 532)$ decreased to -0.7, during strong African dust episodes. Hofer et al. (2017) present an extreme dust event (probably with coarse mode dust dominant) with values of 0.29 ± 0.01 or 0.35 ± 0.01 for $\delta_p(355)$ or $\delta_p(532)$, and values of -0.20 ± 0.13 or 0.29 ± 0.03 for $\mathring{A}_\beta(355, 532)$ or $\mathring{A}_\beta(532, 1064)$, respectively. Freudenthaler et al. (2009) reported 0.31 ± 0.03 and 0.27 ± 0.04 for $\delta_p(532)$ and $\delta_p(1064)$ over Morocco. Haarig et al. (2017a) highlighted maximum values of 0.27 for $\delta_p(1064)$ measured over Barbados, which are almost equal to the coarse dust depolarization ratio. The characteristics of non-dust type can vary widely across regions and times. A review study of Proestakis et al. (2024) suggests a value of 0.05 ± 0.02 at 532 nm for non-dust depolarization ratios (Tesche et al., 2009; Mamouri and Ansmann, 2014, 2016; Marinou et al., 2017; Proestakis et al., 2018). Here we consider 0.05 ± 0.02 for all 3 wavelengths in the synthetic examples and cases where measurements are unavailable. However, such values may be adjusted if measurements become available. Laboratory measurements of dust $\mathring{A}_\beta$ are still missing, thus values from lidar measurements are considered. Mamouri and Ansmann (2014) stated the extinction-related Ångström exponent between 355 and 532 nm to be -0.2, 1.5, 2.0 for coarse dust, fine dust, and non-dust aerosols, respectively. Assuming the same lidar ratios at 355 and 532 nm, these values can be used for the

https://doi.org/10.5194/egusphere-2024-3460
Preprint. Discussion started: 2 January 2025

Table 1. Input parameters used in the synthetic cases (Sect. 2) and case studies (Sect. 3): characteristic depolarization ratios (δ) at 355, 532 or 1064 nm, and backscatter-related Ångström exponent (Å_β) between 355 and 532 nm, or between 532 and 1064 nm, for coarse dust (dc), fine dust (df), and spherical non-dust (nd) aerosols. Typical values are considered from published studies (see text in Sect. 2). Values in parentheses are based on our assumptions.

Aerosol type (abbreviation)	δ(355)	δ(532)	δ(1064)	Å_β(355, 532)	Å_β(532, 1064)
Coarse dust (dc)	0.27 ± 0.03	0.37 ± 0.03	0.27 ± 0.03	-0.2 (± 0.03)	0.3 ± 0.03
Fine dust (df)	0.21 ± 0.02	0.16 ± 0.02	0.09 ± 0.02	1.5 (± 0.03)	0.6 (± 0.03)
Non-dust aerosol (nd)	0.05 ± 0.02	0.05 ± 0.02	0.05 ± 0.02	2.0 (± 0.03)	(1.5 ± 0.03)

$\text{Å}_\beta(355, 532)$. The authors found no available value for $\text{Å}_\beta(532, 1064)$ of fine-mode dust in the literature. Nevertheless, several studies documented range of values of Å_β for the dust layers including the coarse and fine mode dust. For example, Tesche et al. (2009) and Filioglou et al. (2020) found $\text{Å}_\beta(532, 1064)$ values of 0.0 to 0.7, or 0.1 to 0.6, respectively. The upper limit of such range values could be related to the fine-mode dust dominant dust mixture.

It should be emphasized that this paper focuses on presenting a novel methodology, and the investigation of the characteristics is beyond the scope. The characteristic values of the various aerosol types can be readily updated as more accurate values become available and new observations emerge in the field.

2.1 Mixture of two aerosol components

As a first step, a two aerosol component mixture is considered assuming a strongly depolarizing and a weakly depolarizing aerosol types, with type denoted by the subscripts *a* and *b*. The characteristic depolarization ratios of the two aerosol types should be different (i.e., $\delta_a \neq \delta_b$). The total particle backscatter coefficient, β_p, is the sum of the backscatter coefficients of aerosols *a* and *b* ($\beta_p = \beta_a + \beta_b$). The separation method using δ_p from one wavelength, initially developed by Shimizu et al. (2004) and thoroughly discussed in Tesche et al. (2009), is well known and has been widely utilized. In this section, we present an approach for cases where δ_p at two wavelengths are available.

Using Eqs. 1 and 3, the δ_p of the particle ensemble at wavelength λ_1 (or λ_2) can be expressed by Eq. 5 (or 6). A synthetic example is given in Fig. 1(a), using the characteristics of coarse dust and spherical non-dust aerosol from Table 1. Using Eqs. 3 (for wavelengths λ_1 and λ_2) and 4 (for aerosols a and b), the relationships between the aerosol backscatter fractions at two wavelengths can be derived as Eqs. 7 and 8. Therefore, a scatter plot using δ_p at two wavelengths can be generated, and linked to the backscatter fractions (an example is given in Fig. 1b). It is evident that the sum of $\phi_a(\lambda_1)$ and $\phi_b(\lambda_1)$ equals 1 (Eqs. 7–8). Also, the sum of the two aerosol backscatter fractions at λ_2 is equal to 1 (Eq. 9). Eqs. 7–9 remain valid under the interchange of λ_1 and λ_2.

https://doi.org/10.5194/egusphere-2024-3460
Preprint. Discussion started: 2 January 2025

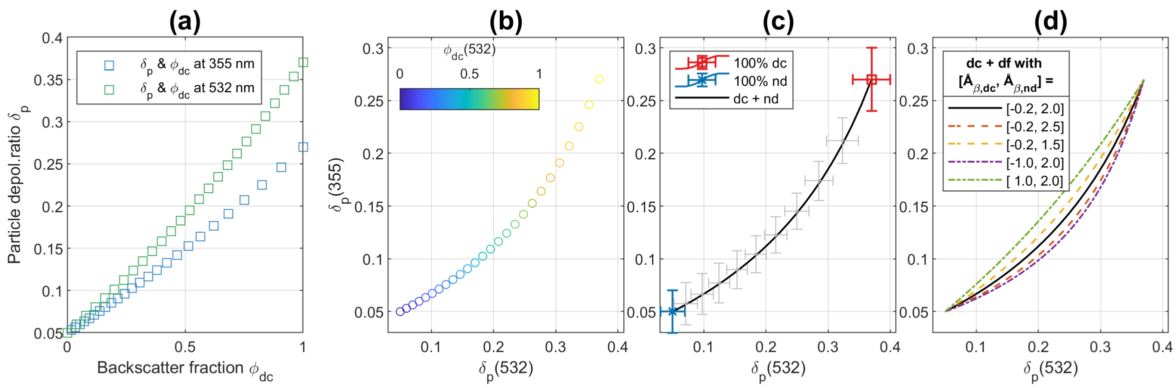

Figure 1. Synthetic particle linear depolarization ratios (δ_p) for the aerosol mixture with two aerosol types: coarse dust (dc) and spherical non-dust aerosol (nd). (a) δ_p against the coarse dust backscatter fraction (ϕ_{dc}) at 355 or 532 nm. (b) Relationship between δ_p at 355 and 532 nm, with ϕ_{dc} at 532 nm shown by color scales. (c) Theoretical characteristic curves of δ_p at 355 and 532 nm for the dc and nd mixture, with uncertainties from Monte Carlo simulations (using parameters in Table 1). (d) Characteristic curves of δ_p at 355 and 532 nm for dc and nd mixture, with different characteristic backscatter-related Ångström exponents ($Å_{\beta,dc}(355,532)$ and $Å_{\beta,nd}(355,532)$).

$$\delta_p(\lambda_1) = \frac{\frac{\phi_a(\lambda_1)\delta_a(\lambda_1)}{\delta_a(\lambda_1)+1} + \frac{\phi_b(\lambda_1)\delta_b(\lambda_1)}{\delta_b(\lambda_1)+1}}{\frac{\phi_a(\lambda_1)}{\delta_a(\lambda_1)+1} + \frac{\phi_b(\lambda_1)}{\delta_b(\lambda_1)+1}} \tag{5}$$

$$\delta_p(\lambda_2) = \frac{\frac{\phi_a(\lambda_2)\delta_a(\lambda_2)}{\delta_a(\lambda_2)+1} + \frac{\phi_b(\lambda_2)\delta_b(\lambda_2)}{\delta_b(\lambda_2)+1}}{\frac{\phi_a(\lambda_2)}{\delta_a(\lambda_2)+1} + \frac{\phi_b(\lambda_2)}{\delta_b(\lambda_2)+1}} \tag{6}$$

$$\phi_a(\lambda_1) = \frac{\eta_a(\lambda_1,\lambda_2)\phi_a(\lambda_2)}{\eta_a(\lambda_1,\lambda_2)\phi_a(\lambda_2) + \eta_b(\lambda_1,\lambda_2)\phi_b(\lambda_2)} \tag{7}$$

$$\phi_b(\lambda_1) = \frac{\eta_b(\lambda_1,\lambda_2)\phi_b(\lambda_2)}{\eta_a(\lambda_1,\lambda_2)\phi_a(\lambda_2) + \eta_b(\lambda_1,\lambda_2)\phi_b(\lambda_2)} \tag{8}$$

$$\phi_a(\lambda_2) + \phi_b(\lambda_2) = 1 \tag{9}$$

In the above-mentioned equations (Eqs. 5–9), eight variables are known: the particle linear depolarization ratios of the particle ensemble ($\delta_p(\lambda_1)$, $\delta_p(\lambda_2)$), and the characteristic depolarization ratios and the backscatter-related Ångström exponents ($\delta_a(\lambda_1)$, $\delta_b(\lambda_1)$, $\delta_a(\lambda_2)$, $\delta_b(\lambda_2)$, $Å_{\beta,a}$, $Å_{\beta,b}$) which are aerosol-type-dependent. Thus, the mathematical relationship between $\delta_p(\lambda_1)$ and $\delta_p(\lambda_2)$ can be derived and expressed through Eq. 10, without unknown parameters. Such a relationship relating to the wavelength dependency on the particle linear depolarization ratios is fixed for the mixture of two aerosol components. The two boundaries are determined by the δ_x of the two aerosols. For the synthetic example in Fig. 1(b-d), the top-right (or left-bottom) boundary of the curve is determined by δ_{dc} (or δ_{nd}) at 355 and 532 nm. $Å_{\beta,x}$ of both aerosol types impacts the curvature of the curve. Examples of characteristic curves using different $Å_{\beta,x}$ values are given in Fig. 1(d) to illustrate the curvature effect: higher $Å_{\beta,nd}$ or lower $Å_{\beta,dc}$ will result in a higher curvature while bending towards the right bottom

https://doi.org/10.5194/egusphere-2024-3460
Preprint. Discussion started: 2 January 2025

direction. A sensitively study on the synthetic example (Fig. 1) was performed based on the Monte Carlo approach. Six variables ($\delta_{dc}(355)$, $\delta_{dc}(532)$, $\mathring{A}_{\beta,dc}$, $\delta_{nd}(355)$, $\delta_{nd}(532)$, $\mathring{A}_{\beta,nd}$) are used, considering normal statistical distribution with their standard derivations (in Table 1). Results using 1000 draws/simulations are shown as gray error bars in Fig. 1(c).

$$\delta_p(\lambda_1) = \frac{\delta_a(\lambda_1)\eta_a[\delta_b(\lambda_1)+1][\delta_a(\lambda_2)+1][\delta_b(\lambda_2)-\delta_p(\lambda_2)] + \delta_b(\lambda_1)\eta_b[\delta_a(\lambda_1)+1][\delta_b(\lambda_2)+1][\delta_p(\lambda_2)-\delta_a(\lambda_2)]}{\eta_a[\delta_b(\lambda_1)+1][\delta_a(\lambda_2)+1][\delta_b(\lambda_2)-\delta_p(\lambda_2)] + \eta_b[\delta_a(\lambda_1)+1][\delta_b(\lambda_2)+1][\delta_p(\lambda_2)-\delta_a(\lambda_2)]} \quad (10)$$

It is concluded that the relationship between δ_p at two wavelengths is not linear, thus, the common use of the ratio of $\delta_p(\lambda_1)$ and $\delta_p(\lambda_2)$ is less accurate than the characteristic curved relationship proposed in this study. Furthermore, these characteristic wavelength dependencies provide the potential application for aerosol typing.

Moreover, there are four independent equations from Eqs. 5–9, considering Eq. 10. Thus, the four unknowns ($\phi_a(\lambda_1)$, $\phi_b(\lambda_1)$, $\phi_a(\lambda_2)$, $\phi_b(\lambda_2)$) can be calculated as a unique solution.

2.2 Mixture of three aerosol components

As a following step, more complicated aerosol mixtures were considered in this section, assuming an aerosol population of three aerosol types (denoted with the subscript *a*, *b* or *c*). The characteristic depolarization ratios (δ_x) of all three types should be different.

Using Eqs. 2 and 3, δ_p of the particle ensemble at wavelength λ_1 (or λ_2) can be expressed by Eq. 11 (or 12). Synthetic examples are given in Fig. 2 for a three aerosol component mixture (coarse dust, fine dust, and spherical non-dust aerosol). δ_p value of the particle ensemble depends on the share of each aerosol type (e.g., Fig. 2a). The pair values of δ_p at two wavelengths must remain within the enclosed region predetermined by three boundary curves, and each curve is determined by the characteristics of any two of three types (e.g., using Eq. 10, see Fig. 1b-d). Similar sensitively study was performed based on the Monte Carlo approach, with results shown in Fig. 2(c), using the characteristic values and uncertainties of δ_x and $\mathring{A}_{\beta,x}$ (in Table 1). The relationships between the aerosol backscatter fractions at two wavelengths can be derived as Eqs. 13–15, and the sum of $\phi_a(\lambda_1)$, $\phi_b(\lambda_1)$, and $\phi_c(\lambda_1)$ is clearly equal to 1. The sum of the three aerosol backscatter fractions at λ_2 is also equal to 1 (Eq. 16). Eqs. 13–16 remain valid under the interchange of λ_1 and λ_2.

https://doi.org/10.5194/egusphere-2024-3460
Preprint. Discussion started: 2 January 2025

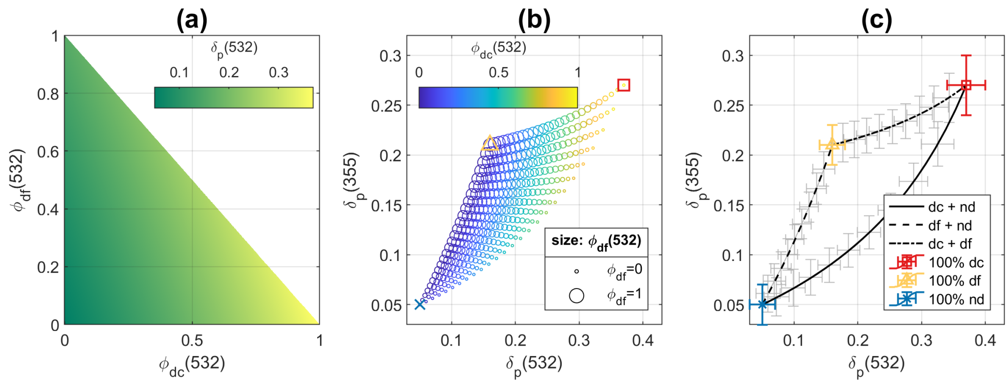

Figure 2. Synthetic particle linear depolarization ratios (δ_p) of the particle ensemble at 355 and 532 nm for the aerosol mixture with three aerosol types: coarse dust (dc), fine dust (df), and spherical non-dust aerosol (nd). (a) δ_p at 532 nm for different backscatter fractions (ϕ) of coarse and fine dust. (b) δ_p at 355 and 532 nm, with coarse dust backscatter fractions (ϕ_{dc}) shown by color scales, and fine dust backscatter fractions (ϕ_{df}) shown by marker sizes. (c) Theoretical characteristic curves of δ_p at 355 and 532 nm for the two aerosol mixtures are in black lines, with uncertainties from Monte Carlo simulations (using parameters in Table 1). The characteristic values of δ_{dc}, δ_{df}, and δ_{nd} is shown as red square, yellow triangle, or blue cross, respectively.

$$\delta_p(\lambda_1) = \frac{\frac{\phi_a(\lambda_1)\delta_a(\lambda_1)}{\delta_a(\lambda_1)+1} + \frac{\phi_b(\lambda_1)\delta_b(\lambda_1)}{\delta_b(\lambda_1)+1} + \frac{\phi_c(\lambda_1)\delta_c(\lambda_1)}{\delta_c(\lambda_1)+1}}{\frac{\phi_a(\lambda_1)}{\delta_a(\lambda_1)+1} + \frac{\phi_b(\lambda_1)}{\delta_b(\lambda_1)+1} + \frac{\phi_c(\lambda_1)}{\delta_c(\lambda_1)+1}} \tag{11}$$

$$\delta_p(\lambda_2) = \frac{\frac{\phi_a(\lambda_2)\delta_a(\lambda_2)}{\delta_a(\lambda_2)+1} + \frac{\phi_b(\lambda_2)\delta_b(\lambda_2)}{\delta_b(\lambda_2)+1} + \frac{\phi_c(\lambda_2)\delta_c(\lambda_2)}{\delta_c(\lambda_2)+1}}{\frac{\phi_a(\lambda_2)}{\delta_a(\lambda_2)+1} + \frac{\phi_b(\lambda_2)}{\delta_b(\lambda_2)+1} + \frac{\phi_c(\lambda_2)}{\delta_c(\lambda_2)+1}} \tag{12}$$

$$\phi_a(\lambda_1) = \frac{\eta_a(\lambda_1,\lambda_2)\phi_a(\lambda_2)}{\eta_a(\lambda_1,\lambda_2)\phi_a(\lambda_2) + \eta_b(\lambda_1,\lambda_2)\phi_b(\lambda_2) + \eta_c(\lambda_1,\lambda_2)\phi_c(\lambda_2)} \tag{13}$$

$$\phi_b(\lambda_1) = \frac{\eta_b(\lambda_1,\lambda_2)\phi_b(\lambda_2)}{\eta_a(\lambda_1,\lambda_2)\phi_a(\lambda_2) + \eta_b(\lambda_1,\lambda_2)\phi_b(\lambda_2) + \eta_c(\lambda_1,\lambda_2)\phi_c(\lambda_2)} \tag{14}$$

$$\phi_c(\lambda_1) = \frac{\eta_c(\lambda_1,\lambda_2)\phi_c(\lambda_2)}{\eta_a(\lambda_1,\lambda_2)\phi_a(\lambda_2) + \eta_b(\lambda_1,\lambda_2)\phi_b(\lambda_2) + \eta_c(\lambda_1,\lambda_2)\phi_c(\lambda_2)} \tag{15}$$

$$\phi_a(\lambda_2) + \phi_b(\lambda_2) + \phi_c(\lambda_2) = 1 \tag{16}$$

It is possible to retrieve the six unknowns $\phi_x(\lambda_i)$ (with x being a, b, or c, and i being 1 or 2) using the six independent equations (Eqs. 11–16) with a unique mathematical solution. For the sake of simplicity, an aerosol-type-dependent term, Q_x, was introduced, which is based on the characteristic depolarization ratio (δ_x), as well as the particle linear depolarization ratio of the particle ensemble (δ_p), at a given wavelength (Eq. 17). For three aerosol types and depolarization ratios at two wavelengths, there are six $Q_x(\lambda_i)$. Thus, the Eq. 11 or 12 can be simplified as Eq. 18. The expressions of the aerosol backscatter fraction $\phi_x(\lambda_i)$ can be mathematically derived using Eqs. 13–18. An example of the expression of $\phi_a(\lambda_2)$ solution is given in Eq. 19. The solution equations for the other two types can apply the same equation, with the indices a, b, and c interchanged

https://doi.org/10.5194/egusphere-2024-3460
Preprint. Discussion started: 2 January 2025

accordingly. The aerosol backscatter coefficient of one type can be easily calculated from the total backscatter coefficient using the backscatter fraction.

$$Q_x(\lambda_i) = \frac{\delta_p(\lambda_i) - \delta_x(\lambda_i)}{\delta_x(\lambda_i) + 1} \tag{17}$$

$$\phi_a(\lambda_i)Q_a(\lambda_i) + \phi_b(\lambda_i)Q_b(\lambda_i) + \phi_c(\lambda_i)Q_c(\lambda_i) = 0 \tag{18}$$

$$\phi_a(\lambda_2) = \frac{\eta_b Q_b(\lambda_1)Q_c(\lambda_2) - \eta_c Q_c(\lambda_1)Q_b(\lambda_2)}{\eta_a Q_a(\lambda_1)[Q_b(\lambda_2) - Q_c(\lambda_2)] + \eta_b Q_b(\lambda_1)[Q_c(\lambda_2) - Q_a(\lambda_2)] + \eta_c Q_c(\lambda_1)[Q_a(\lambda_2) - Q_b(\lambda_2)]} \tag{19}$$

2.3 Uncertainty study

Decomposition of two aerosol component mixture is well studied and reported in many studies. In this section, we present a sensitivity study and explore the uncertainties of the proposed methodology for the decomposition of three aerosol component mixture using particle depolarization ratios at two wavelengths.

In the simulation, synthetic data representing aerosol mixtures, which may include coarse dust, fine dust, and spherical non-dust aerosol, are utilized with characteristics from Table 1. The pair values of δ_p of the aerosol mixture, with whichever the mixing ratio of the three components, should be inside the region bounded by the three characteristic curves. The uncertainties of both the type-specific characteristics and the measured δ_p introduce uncertainties on the retrievals of the aerosol backscatter fractions. Here, we first focus on the uncertainty source of the type-specific characteristics and omit the uncertainty of the measured δ_p.

Three representative cases are manually selected, with initial δ_p values given in Table 2 and Fig. 3(a). The aerosol backscatter fractions can be calculated using Eq. 19, where there are two measured/initial parameters (δ_p at 355 and 532 nm), and nine variables ($\delta_{dc}(355)$, $\delta_{dc}(532)$, $Å_{\beta,dc}$, $\delta_{df}(355)$, $\delta_{df}(532)$, $Å_{\beta,df}$, $\delta_{nd}(355)$, $\delta_{nd}(532)$, $Å_{\beta,nd}$). The idea results without introducing uncertainties are given as "Reference results" in Table 2. A Monte Carlo simulation was conducted involving 10000 draws based on normal distributions of nine variables (Table 1). For each draw, the aerosol backscatter fractions of three components are calculated, resulting the distributions shown in Fig. 3(b-d). The statistical parameters are given in Table 2, where skewness is a measure of the asymmetry of the distribution, and kurtosis is a measure of the flatness of the distribution compared to a normal distribution. The retrieved ϕ_x distributions are also presented as ternary plots in Fig. 3(e), where the color scale represent the frequency of occurrences. We can easily identify areas where there is a greater accuracy/confidence for the ϕ_x retrievals with darker color.

For case 1, the pair values of δ_p locate in the middle of the enclosed characteristic region. The retrieved backscatter fractions are closer in shape to a Gaussian distribution than the other two cases. The values are reasonably between 0 to 1. $\delta_p(355)$ and $\delta_p(532)$ of case 2 are located inside the error bars of the characteristic curve of coarse dust and non-dust aerosol. Thus, for this

https://doi.org/10.5194/egusphere-2024-3460
Preprint. Discussion started: 2 January 2025

Table 2. Parameters for the uncertainty study. Three cases with different initial particle linear depolarization ratios (δ_p) of the particle ensemble at 355 and 532 nm are used. Reference results are calculated using Eq. 19 without introducing uncertainties. Statistical parameters of retrieved aerosol backscatter fraction ϕ_x of coarse dust (dc), fine dust (df), and non-dust aerosol (nd) are given after Monte Carlo simulations.

	Initial δ_p		Reference results		Monte Carlo results			
	$\delta_p(355)$	$\delta_p(532)$			Mean	Standard deviation	Skewness	Kurtosis
Case 1	0.16	0.19	$\phi_{dc}(532)$	0.33	0.33	0.09	0.53	13.63
			$\phi_{df}(532)$	0.42	0.42	0.15	-1.78	51.61
			$\phi_{nd}(532)$	0.25	0.25	0.07	3.31	107.97
Case 2	0.18	0.28	$\phi_{dc}(532)$	0.74	0.76	0.14	1.84	95.39
			$\phi_{df}(532)$	0.08	0.05	0.20	-0.96	119.17
			$\phi_{nd}(532)$	0.19	0.19	0.08	-0.62	92.74
Case 3	0.10	0.30	$\phi_{dc}(532)$	1.01	1.05	0.38	57.08	4527.20
			$\phi_{df}(532)$	-0.46	-0.52	0.59	-53.35	3906.65
			$\phi_{nd}(532)$	0.45	0.47	0.24	36.50	2010.26

δ_p pair, it is possible that the mixture contains only coarse dust and non-dust aerosol, or contains three aerosol components. For example, a small part of simulated values of ϕ_{df} distribution in Fig. 3(c) is negative due to the uncertainties. In case 3, the pair values of δ_p are far away from the characteristic region, only un-physical values (always below 0) were derived for ϕ_{df} (Fig. 3d), and a big portion of ϕ_{dc} are bigger than 1. This case is clearly not a mixture of above mentioned three aerosol components. It could contain other depolarizing particles, e.g., pollen, in the mixture.

As a second step, we concentrate on the random uncertainties on the measured δ_p. Reference values of ϕ_{dc}, ϕ_{df}, and ϕ_{nd} of three cases in Table 2 are used here as inputs. Note that it is purely a mathematical problem, as the system can be solved regardless of whether the values are physically meaningful (e.g., case 3). $\delta_p(355)$ and $\delta_p(532)$ are derived using Eqs. 11–15, and they exactly match the initial values. We added several relative uncertainty levels on both $\delta_p(355)$ and $\delta_p(532)$ from 0 % to 30 %, and performed Monte Carlo simulations using 10000 draws for each level, considering normal statistical distributions. The uncertainties (including bias and standard deviations) and relative uncertainties on the retrieved ϕ_x for three cases are shown in Fig. 4, and they increase as the uncertainties on δ_p increase. Such uncertainties on ϕ_x range from 0.02 to 0.18 when considering typical relative uncertainties on the δ_p of 5–10 %. There is the demand of well characterized lidar systems to deliver high-quality depolarization ratios.

3 Case studies of mineral dust

In this section, the algorithm was applied to lidar observations of dust at different regions.

https://doi.org/10.5194/egusphere-2024-3460
Preprint. Discussion started: 2 January 2025

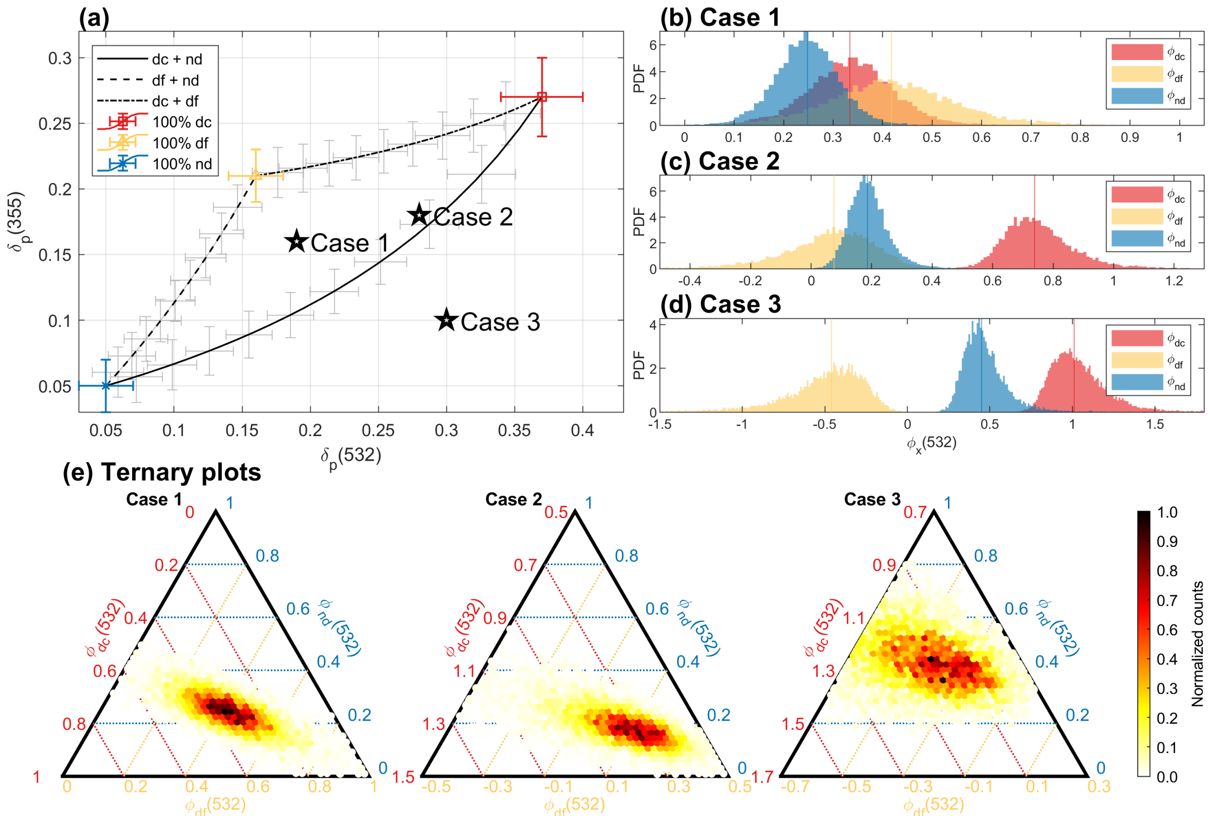

Figure 3. (a) Theoretical characteristic curves of δ_p at 355 and 532 nm for the 2 aerosol mixtures are in black, with uncertainties from Monte Carlo simulations (using parameters in Table 1). The characteristic δ_x of coarse dust (dc), fine dust (df), or spherical non-dust (nd) aerosol are shown as red square, yellow triangle, or blue cross, respectively. (b-d) Probability density function (PDF) estimates of the backscatter fractions (ϕ_x) of dc, df, and nd aerosol, for each case. Monte Carlo approach was applied. (e) Ternary plots of characteristic ϕ_x for 3 cases, with normalized counts shown as color.

3.1 Arabian dust

Filioglou et al. (2020) reported the aerosol particle properties of Arabian dust over a rural site in the United Arab Emirates, during the 1 year measurement campaign between March 2018 and February 2019, within the framework of the Optimization of Aerosol Seeding In rain enhancement Strategies (OASIS) project. Among 1130 night-time aerosol particle layers, δ_p at both 355 and 532 nm are available for 1063 layers. These layer-mean δ_p are plotted in Fig. 5, with center mass of the layers shown by color scale, and layer depths shown by marker sizes.

The measurement site is a receptor of frequent dust events, three possible aerosol types are assumed to be present in these layers: coarse and fine dust (with characteristics in Table 1), and the spherical non-dust aerosols with anthropogenic and/or marine origin. From the lidar measurements, the mean values of the depolarization ratios for the non-dust aerosols (δ_{nd}) are

https://doi.org/10.5194/egusphere-2024-3460
Preprint. Discussion started: 2 January 2025

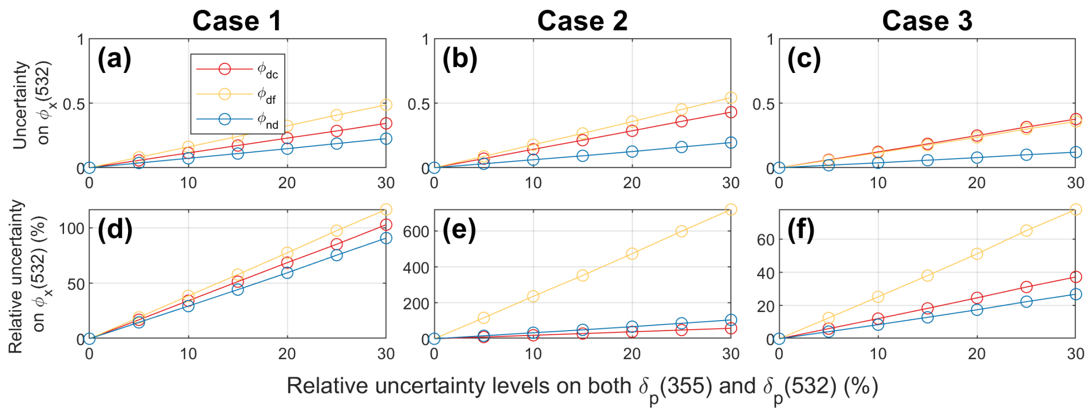

Figure 4. Estimated uncertainties (a–c) and relative uncertainties (d–f) on the retrieved backscatter fractions (ϕ_x) at 532 nm of coarse dust (dc), fine dust (df), or spherical non-dust (nd) aerosols, against the applied relative uncertainties on the particle linear depolarization ratios at both 355 and 532 nm ($\delta_p(355)$ and $\delta_p(532)$). Monte Carlo approach was applied.

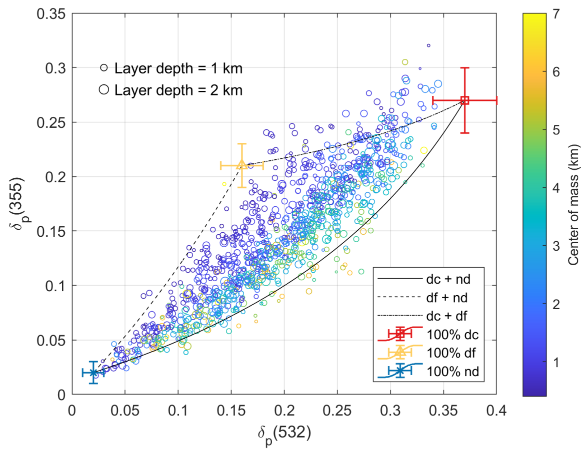

Figure 5. Scatter plot of layer-mean particle linear depolarization ratios (δ_p) of the particle ensemble at 355 and 532 nm of Arabian dust layers observed over United Arab Emirates. The altitude of the center of mass of the layers are shown by color scale, and layer depths shown by marker sizes. Theoretical characteristic curves of δ_p at 355 and 532 nm for the two aerosol mixtures are in black lines. Characteristic δ_x of coarse dust (dc), fine dust (df), or spherical non-dust (nd) aerosol is shown as red square, yellow triangle, or blue cross, respectively.

derived as 0.02 ± 0.01 at both 355 and 532 nm. $\mathring{A}_{\beta,nd}$ is assumed as 2 (cf., Table 1). The majority of the cases are well within the boundaries defined by the characteristic values of the three-aerosol-component method. A few δ_p pairs are above the characteristic curve of coarse and fine dust. This could be an indication that the δ_x at 355 nm for pure Arabian dust (for both coarse and fine mode) may have slightly higher values. It may also be that the commonly reported layer-mean values which are

https://doi.org/10.5194/egusphere-2024-3460
Preprint. Discussion started: 2 January 2025

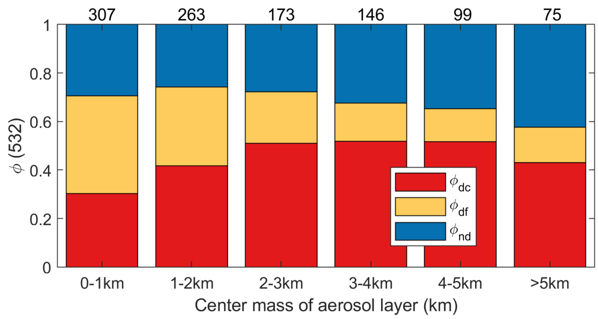

Figure 6. Height-dependent aerosol backscatter fractions ($\phi_x(532)$) of coarse dust (dc), fine dust (df), and non-dust (nd) aerosol, for Arabian dust layers observed over United Arab Emirates. Layer numbers are given on the top.

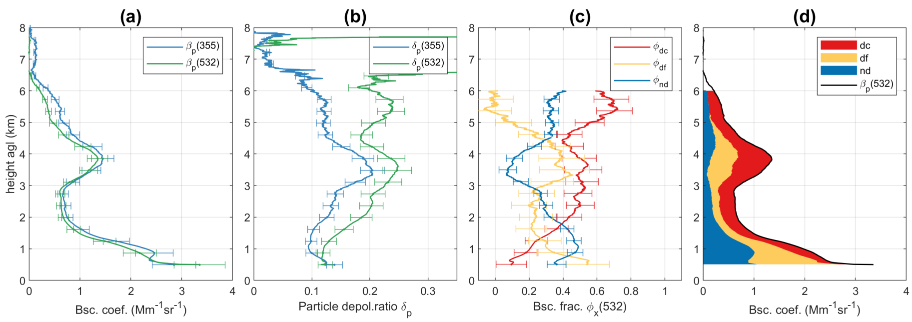

Figure 7. An example of lidar-derived optical profiles (time-averaged at 00:10–01:09 on 4 August 2018 over United Arab Emirates). (a) Particle backscatter coefficients and (b) particle linear depolarization ratio (δ_p) at 355 and 532 nm. (c) The retrieved backscatter fractions (ϕ) of coarse dust (dc), fine dust (df), and non-dust (nd) aerosols at 532 nm, with uncertainties (shown by error bars) calculated using Monte Carlo approach following method in Sect. 2.3. (d) Separation of 3 aerosol backscatter coefficients at 532 nm.

often calculated using smoothed optical parameters may lower the true characteristic value of dust particles. To this direction, measuring the characteristics of pure dust particles, e.g., in laboratory experiments, would be beneficial.

The aerosol backscatter fractions of the three aerosol components are calculated using Eq. 19. δ_p pairs located outside the region may result in negative or values above one for ϕ_x. To avoid introducing a bias, these negative or above one values are included in the analysis, as a large dataset is utilized. Final values of $\phi_x(532)$ are grouped using the center mass of aerosol layers and shown in Fig. 6. The non-dust aerosol contribution is increasing the higher the aerosol layer is in the atmosphere and at the same time the fine dust contribution is decreasing. Coarse dust contributes more at heights between 2 to 5 km, which is in line with Fig. 7 of Filioglou et al. (2020) where higher δ_p at 532 nm has been detected. An example of vertical profiles is given in Fig. 7. The fine dust and the non-dust aerosols dominant the lowest layer below 1.5 km. The lofted layer between 3 and 4.5 km presents enhanced δ_p, containing mainly coarse and fine dust. A higher disparity between δ_p at 355 and 532 nm was found for an upper layer between 5 and 6 km, revealing a mixture of coarse dust and non-dust aerosol particles.

https://doi.org/10.5194/egusphere-2024-3460
Preprint. Discussion started: 2 January 2025

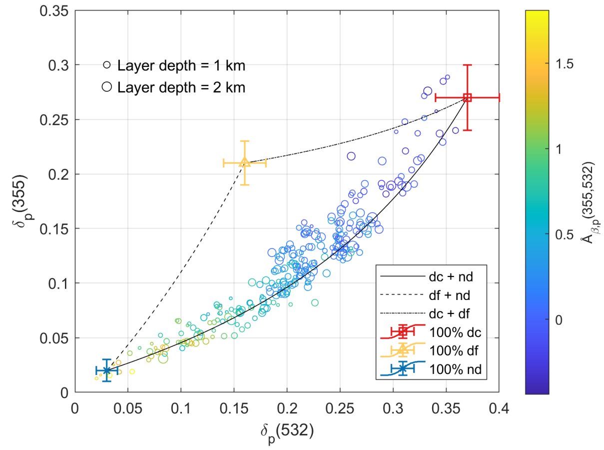

Figure 8. Scatter plot of layer-mean particle linear depolarization ratios (δ_p) of the particle ensemble at 355 and 532 nm of Central Asian dust layers observed over Dushanbe. The layer-mean backscatter-related Ångström exponents ($Å_{\beta,p}$) are shown by color scale, and the layer depths by marker sizes. Theoretical characteristic curves of δ_p at 355 and 532 nm for the 2 aerosol mixtures are in black. Characteristic δ_x of coarse dust (dc), fine dust (df), or spherical non-dust (nd) aerosols are shown as red square, yellow triangle, or blue cross, respectively.

3.2 Asian dust

Central Asia is one of the hot spot regions facing significant environmental challenges and climate-change effects. Hofer et al. (2020) presented a dense data set of lidar observations for a Central Asian site during the 18 month campaign from March 2015 to August 2016, at Dushanbe, Tajikistan, in the framework of the Central Asian Dust EXperiment (CADEX) project. They found broad distributions of optical properties of the 276 aerosol layers, reflecting the occurrence of very different aerosol conditions with aerosol mixtures consisting of mineral dust, soil dust, and anthropogenic pollution.

Layer mean δ_p at 355 and 532 nm are shown in Fig. 8, with the layer mean $Å_{\beta,p}$ shown by color scale, and the layer depths by marker sizes. As already discussed in Hofer et al. (2020), with decreasing extinction-related Ångström exponents, the δ_p at two wavelengths increase. For the aerosol component separations, we considered three aerosol types in those layers: coarse and fine dust (with characteristics in Table 1), and non-dust aerosols. Hofer et al. (2020) derived the mean values of δ_{nd} as 0.02 $\pm$ 0.01 or 0.03 $\pm$ 0.01 at 355 or 532 nm, respectively. $Å_{\beta,nd}$ is assumed as 2 (cf., Table 1). The pair values of δ_p are mostly located close to the characteristic curve of coarse dust and non-dust aerosol. The aerosol backscatter fractions are calculated (Eq. 19) and shown in Fig. 9, as time series. Highest dust contributions were found during the summer season, with coarse (or fine) dust contributes 61 % (or 8 %) on the backscatter coefficients at 532 nm. During spring and autumn, dust (including coarse and fine mode) and non-dust aerosols have nearly equal contributions. Only during winter months, non-dust (e.g., urban haze) dominates with 75 % on the backscatter coefficients.

Hu et al. (2020) documented 1 month East Asia dust aerosol observations over Kashi, China, in April 2019. The dust particles originate mainly from the Taklamakan desert. The measured δ_p of dust layers are about 0.28–0.32 $\pm$ 0.07, 0.36 $\pm$ 0.05, and

https://doi.org/10.5194/egusphere-2024-3460
Preprint. Discussion started: 2 January 2025

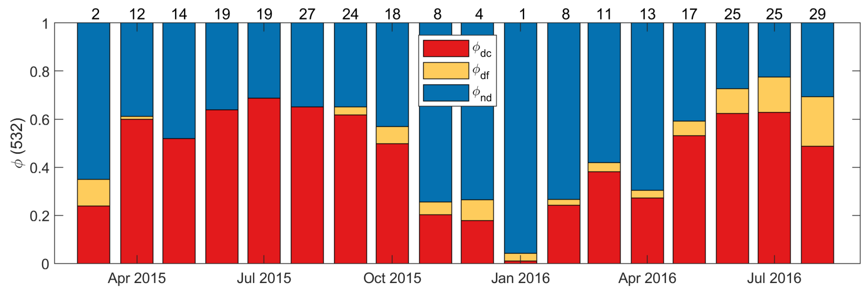

Figure 9. Monthly means of aerosol backscatter fractions ($\phi_x(532)$) of coarse dust (dc), fine dust (df), and non-dust (nd) aerosol, for Central Asian dust layers observed over Dushanbe. Layer numbers are given on the top.

0.31 ± 0.05 at 355, 532, and 1064 nm, respectively. These δ_p are higher than the typical values of Asian dust in the literature (Murayama et al., 2004; Dieudonné et al., 2015; Hofer et al., 2017). The reason could be linked to the fact that observations were near the dust source region, and there would be a large fraction of coarse and giant dusts particles. They described four representative cases with six dust layers. The δ_p values of two pure dust layers are 0.32 at 355 nm and 0.31 at 1064 nm, which are higher than the characteristic depolarization ratios of coarse dust (0.27 at 355 nm and 0.27 at 1064 nm in Table 1). For the four polluted dust layers, two of them have higher δ_p at 355 nm and 1064 nm compared to the δ_{dc}. Those values make the application of the algorithm unsuitable, as the δ_p pairs locate outside the characteristic region, hence, the results would yield some un-physical values (below zero or above one as the fraction). The characteristic depolarization ratios of Taklamakan desert dust need to be determined, especially at wavelengths 355 and 1064 nm. The inclusion of giant dust particles may have impact on the characteristic depolarization ratios of coarse dust type when performing the decomposition.

3.3 Saharan dust

Many research studies have explored the geometric and optical characteristics of Saharan dust layers through lidar observations (e.g., Groß et al., 2011; Ansmann et al., 2003; Groß et al., 2015; Szczepanik et al., 2021). In this section, available lidar observations of the Saharan dust depolarization ratios at all three classical lidar wavelengths (355, 532 and 1064 nm) are considered. The small and spherical particles affect the back-scattering at shorter wavelengths more effectively than at longer wavelengths, whereas longer wavelengths are more sensitive to large particles.

Haarig et al. (2022) (referred as Ha22 further on) reported two case studies of Saharan dust layers observed over Leipzig, Germany. In the first pure-dust case in February 2021, Saharan dust plumes reached the observation station in less than 2 d after emission, exhibiting δ_p of 0.242 ± 0.024, 0.299 ± 0.018 and 0.206 ± 0.010 at 355, 532 and 1064 nm, respectively. In the second polluted-dust case in March 2021, the dust spent about 1 week in transportation, and the dust plume mixed with European haze. Such dust layers have δ_p of 0.174 ± 0.041, 0.298 ± 0.016 and 0.242 ± 0.007 at 355, 532 and 1064 nm, respectively. Haarig et al. (2017a) (referred as Ha17) documented the lidar observations in Saharan dust layers over Barbados in the summer seasons of 2013 and 2014, in the framework of the Saharan Aerosol Long-range Transport and Aerosol-Cloud-

https://doi.org/10.5194/egusphere-2024-3460
Preprint. Discussion started: 2 January 2025

Interaction Experiment (SALTRACE). δ_p for long-range-transported (after approximately 1 week transport over the tropical Atlantic) Saharan dust layers were found to be 0.252 ± 0.030, 0.280 ± 0.020, 0.225 ± 0.022 at 355, 532 and 1064 nm, respectively. Hu (2018) (referred as Hu18) described two cases of lidar measurements of long-range-transported Saharan dust observed at ATOLL observatory in Lille, France. The value ranges of δ_p were 0.25–0.26 (0.25–0.27), 0.25–0.28 (0.24–0.26), 0.17–0.21 (0.20–0.22) at 355, 532, 1064 nm for the first case in March 2017 (or the second case in October 2017), respectively.

The pair values of δ_p of these cases are presented in Fig. 10 to investigate the aerosol mixing states. We assume that there are coarse dust (dc), fine dust (df), and non-dust (nd) aerosols in the mixture, with characteristic values of δ_x and $Å_{\beta,x}$ as given in Tables 1. The characteristics of background non-dust aerosols for these cases are different, but here we consider them as the same for the simplification. The two cases of Ha22 are located well on the characteristic curves of dc & df, or dc & nd, respectively, for δ_p pairs both at 532 & 355 nm (Fig. 10a), and at 532 & 1064 nm (Fig. 10b). In the first case, dust plumes were directly transported towards to the station, thus, only dust (both coarse and fine mode) is contained within the observed plume. In the second case, δ_p reveal the impact of aerosol pollution mixed into the dust layers after the transportation, and it seems that the remaining dust are mainly coarse mode. The other three cases of Ha17 and Hu18 are mostly located around the characteristic curve of dc & df considering δ_p pairs at 355 & 532 nm (Fig. 10a), or located inside the enclosed characteristic region of three types regarding δ_p pairs at 532 & 1064 nm (Fig. 10b). It should be noted that the values reported by Ha17 are the average over 21 individual cases of long-range-transported dust.

Apart from the first case of Ha22, all cases were long-range-transported dust. Results reveal that coarse dust contribute a lot in these layers. The dust particle size distribution can change quickly because of the dry deposition (e.g., gravitational settling). However, observations have consistently shown that coarse dust, or even giant dust, are able to transport much farther than previously expected, and can have longer atmospheric lifetime (e.g., Mallios et al., 2021; Ryder et al., 2018, 2019; van der Does et al., 2018; Denjean et al., 2016).

4 Conclusions

Polarization-based algorithms have been developed and wildly used for the decomposition of two aerosol components. The two-step POLIPHON method allows separating three aerosol components under the assumption about the spherical particle fraction. The measurements of depolarization ratios at multiple wavelengths from a single or multiple lidars have become increasingly common, with availability continuing to expand. In this study, we present an extended methodology, using the particle linear depolarization ratios measured at two wavelengths, for the decomposition of three aerosol components, to retrieve the aerosol-type-specific backscatter fractions. This algorithm can be utilized for an almost unambiguous separation of aerosol components, on the condition that their characteristic depolarization ratios are different. And it requires the proper knowledge of characteristic depolarization ratios and backscatter-related Ångström exponent of each aerosol type. Therefore, laboratory and modeling studies, or for a layer with only one aerosol component in atmospheric conditions, to characterize pure particles would be beneficial, and increase the accuracy for the retrievals. Furthermore, a good characterization of the lidar system is necessary to provide the depolarization ratio with a small uncertainty. The relationship between particle

https://doi.org/10.5194/egusphere-2024-3460
Preprint. Discussion started: 2 January 2025

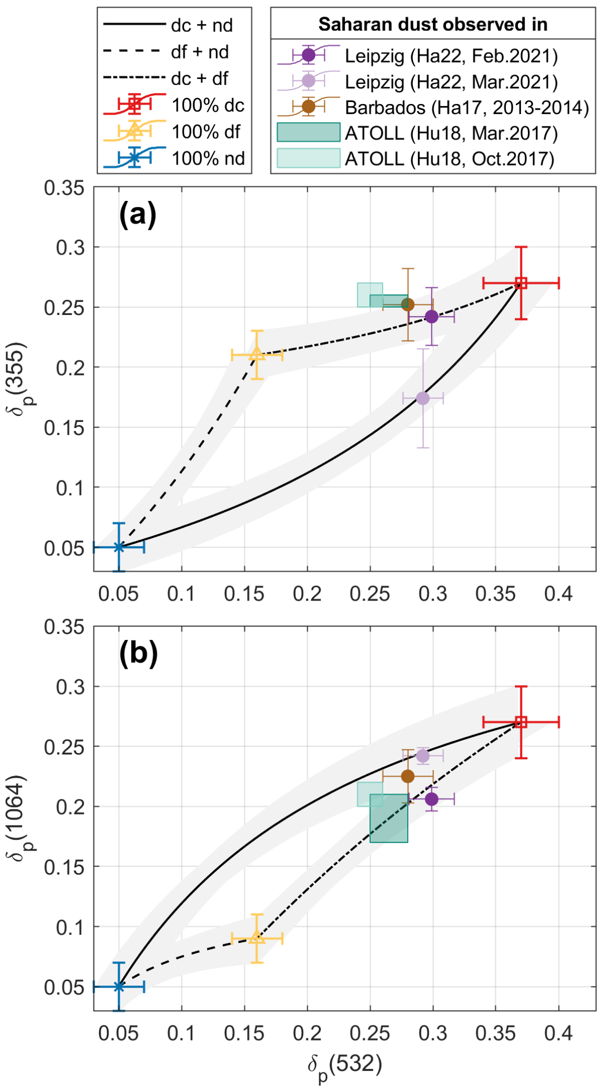

Figure 10. Scatter plot of layer-mean particle linear depolarization ratios (δ_p) of the particle ensemble (a) at 355 and 532 nm, or (b) at 532 and 1064 nm of Saharan dust layers observed in different places: Ha22 – Haarig et al. (2022), Ha17 – Haarig et al. (2017a), Hu18 – Hu (2018). Theoretical characteristic curves of δ_p for the two aerosol mixtures are in black lines, with uncertainties shown as shaded area from Monte Carlo simulations (using parameters in Table 1). Characteristic δ_x of coarse dust (dc), fine dust (df), or spherical non-dust (nd) aerosol are shown as red square, yellow triangle, or blue cross, respectively.

linear depolarization ratios at two wavelengths for a mixture of two and three aerosol components has been mathematically investigated: the pair values must locate on the characteristic curved line (for two aerosol components) or remain within the enclosed region predetermined by three boundary characteristic curves (for three aerosol components). A characteristic curve

https://doi.org/10.5194/egusphere-2024-3460
Preprint. Discussion started: 2 January 2025

line has its boundaries determined by the characteristic depolarization ratios and its curvature influenced by the characteristic backscatter-related Ångström exponents of two aerosol types.

The present algorithm has been applied to synthetic examples considering dust mixtures and to lidar observations of Arabian dust, Asian dust, and Saharan dust, based on the dust characteristics reported in numerous laboratory and field studies. The backscatter fractions of coarse-mode dust (>1 μm in diameter), fine-mode dust (<1 μm in diameter), and spherical non-dust aerosols were retrieved, which can be converted to the aerosol-type-specific backscatter coefficients, and extinction coefficients (or aerosol optical depth) with known lidar ratios. These results can be further utilized to estimate the vertical profiling of mass concentration, cloud condensation nucleus (CCN) and ice-nucleating particle (INP) concentrations (Mamouri and Ansmann, 2016, 2017). It seems that for the Arabian dust and East Asia dust, the characteristic depolarization ratios at 355 nm for pure fine and pure coarse mode dust were underestimated. On the other hand, in Central Asia, the fine mode dust depolarization ratio at 355 nm could be lower to have more fine mode contribution. Regional differences in the pure dust depolarization ratios should be investigated in future. Other than dust mixture, it would be also possible for the decomposition of an aerosol mixture containing other types of 3 aerosol components. For example, an aerosol mixture with spherical background particles, and two types of pollen (e.g., birch and pine pollen with different characteristic depolarization ratios, Shang et al., 2020; Filioglou et al., 2023). However, additional dedicated laboratory studies for the pollen characterization are desirable. Furthermore, dry marine aerosols (Haarig et al., 2017b; Ferrare et al., 2023), and stratospheric smoke aerosols (Haarig et al., 2018; Hu et al., 2019) also show enhanced depolarization ratios with certain spectral slopes, indicating that the algorithm is applicable to aerosol mixtures containing these types as well.

Code and data availability. All data used are from published literature, and are available upon request. The algorithm code is available: https://github.com/xxshang/Shang-et-al_2025_Decomposition-of-three-aerosol-components.

Author contributions. XS developed the algorithm, conceptualized the study, analyzed data, and wrote the paper. MF, JH, MH, QH, PG analyzed and ensured the high-quality lidar data. SR and MK provided guidance of the study. All authors were involved in editing the paper, interpreting the results, and the discussion of the manuscript.

Competing interests. The authors declare that they have no conflict of interest.

Acknowledgements. This research has been supported by the Academy of Finland (projects nos. 329216). This project has received funding from Horizon Europe programme under Grant Agreement No 101137680 via project CERTAINTY (Cloud-aERosol inTeractions & their impActs IN The earth sYstem). We acknowledge the support by the National Center of Meteorology, Abu Dhabi, UAE, under the UAE Research Program for Rain Enhancement Science, for the Optimization of Aerosol Seeding In rain enhancement Strategies (OA-

https://doi.org/10.5194/egusphere-2024-3460
Preprint. Discussion started: 2 January 2025

SIS) project. We would also like to thank Timo Anttila and Siddharth Tampi for providing on-site technical support during OASIS project. The CADEX project for first lidar measurements in Tajikistan was funded by the German Federal Ministry of Education and Research (BMBF) in the context of “Partnerships for sustainable problem solving in emerging and developing countries” (grant no. 01DK14014). The project PoLiCyTa to setup the new lidar system in Dushanbe is also funded by BMBF under the grant number 01LK1603A. Lidar measurements in Tajikistan would not have been possible without support of the Academy of Sciences of the Republic of Tajikistan. We want to thank Sabur F. Abdullaev and Abduvosit N. Makhmudov for their support in Tajikistan, and Dietrich Althausen, Ronny Engelmann and Holger Baars for their tireless efforts to enable lidar observations in Tajikistan. The lidar observations also received funding from ACTRIS-D funded by BMBF under grant agreements 01LK2001A and 01LK2002A under the FONA Strategy “Research for Sustainability”. We acknowledge Labex CaPPA, CPER CLIMIBIO and OBS4CLIM for the financial support to lidar observations and research activities at ATOLL observatory, France. We thank Ulrich Theune for the MATLAB File Exchange code of Ternary plots (Ulrich Theune (2024). Ternary Plots (https://www.mathworks.com/matlabcentral/fileexchange/7210-ternary-plots), MATLAB Central File Exchange. Retrieved October 24, 2024.).

References

Adebiyi, A., Kok, J. F., Murray, B. J., Ryder, C. L., Stuut, J.-B. W., Kahn, R. A., Knippertz, P., Formenti, P., Mahowald, N. M., Pérez García-Pando, C., Klose, M., Ansmann, A., Samset, B. H., Ito, A., Balkanski, Y., Di Biagio, C., Romanias, M. N., Huang, Y., and Meng, J.: A review of coarse mineral dust in the Earth system, Aeolian Research, 60, 100 849, https://doi.org/10.1016/j.aeolia.2022.100849, 2023.

Ansmann, A., Bösenberg, J., Chaikovsky, A., Comerón, A., Eckhardt, S., Eixmann, R., Freudenthaler, V., Ginoux, P., Komguem, L., Linné, H., Márquez, M. L., Matthias, V., Mattis, I., Mitev, V., Müller, D., Music, S., Nickovic, S., Pelon, J., Sauvage, L., Sobolewsky, P., Srivastava, M. K., Stohl, A., Torres, O., Vaughan, G., Wandinger, U., and Wiegner, M.: Long-range transport of Saharan dust to northern Europe: The 11–16 October 2001 outbreak observed with EARLINET, Journal of Geophysical Research: Atmospheres, 108, https://doi.org/10.1029/2003JD003757, 2003.

Ansmann, A., Tesche, M., Seifert, P., Groß, S., Freudenthaler, V., Apituley, A., Wilson, K. M., Serikov, I., Linné, H., Heinold, B., Hiebsch, A., Schnell, F., Schmidt, J., Mattis, I., Wandinger, U., and Wiegner, M.: Ash and fine-mode particle mass profiles from EARLINET-AERONET observations over central Europe after the eruptions of the Eyjafjallajökull volcano in 2010, Journal of Geophysical Research: Atmospheres, 116, https://doi.org/10.1029/2010JD015567, 2011.

Ansmann, A., Seifert, P., Tesche, M., and Wandinger, U.: Profiling of fine and coarse particle mass: case studies of Saharan dust and Eyjafjallajökull/Grimsvötn volcanic plumes, Atmospheric Chemistry and Physics, 12, 9399–9415, https://doi.org/10.5194/acp-12-9399-2012, 2012.

Ansmann, A., Mamouri, R.-E., Hofer, J., Baars, H., Althausen, D., and Abdullaev, S. F.: Dust mass, cloud condensation nuclei, and ice-nucleating particle profiling with polarization lidar: updated POLIPHON conversion factors from global AERONET analysis, Atmospheric Measurement Techniques, 12, 4849–4865, https://doi.org/10.5194/amt-12-4849-2019, 2019.

Baars, H., Kanitz, T., Engelmann, R., Althausen, D., Heese, B., Komppula, M., Preißler, J., Tesche, M., Ansmann, A., Wandinger, U., Lim, J.-H., Ahn, J. Y., Stachlewska, I. S., Amiridis, V., Marinou, E., Seifert, P., Hofer, J., Skupin, A., Schneider, F., Bohlmann, S., Foth, A., Bley, S., Pfüller, A., Giannakaki, E., Lihavainen, H., Viisanen, Y., Hooda, R. K., Pereira, S. N., Bortoli, D., Wagner, F., Mattis, I., Janicka, L., Markowicz, K. M., Achtert, P., Artaxo, P., Pauliquevis, T., Souza, R. A. F., Sharma, V. P., van Zyl, P. G., Beukes, J. P., Sun, J., Rohwer, E. G., Deng, R., Mamouri, R.-E., and Zamorano, F.: An overview of the first decade of Polly^{NET}: an emerging network of automated Raman-polarization lidars for continuous aerosol profiling, Atmospheric Chemistry and Physics, 16, 5111–5137, https://doi.org/10.5194/acp-16-5111-2016, 2016.

Bohlmann, S., Shang, X., Vakkari, V., Giannakaki, E., Leskinen, A., Lehtinen, K. E. J., Pätsi, S., and Komppula, M.: Lidar depolarization ratio of atmospheric pollen at multiple wavelengths, Atmospheric Chemistry and Physics, 21, 7083–7097, https://doi.org/10.5194/acp-21-7083-2021, 2021.

Burton, S. P., Hair, J. W., Kahnert, M., Ferrare, R. A., Hostetler, C. A., Cook, A. L., Harper, D. B., Berkoff, T. A., Seaman, S. T., Collins, J. E., Fenn, M. A., and Rogers, R. R.: Observations of the spectral dependence of linear particle depolarization ratio of aerosols using NASA Langley airborne High Spectral Resolution Lidar, Atmospheric Chemistry and Physics, 15, 13 453–13 473, https://doi.org/10.5194/acp-15-13453-2015, 2015.

Castellanos, P., Colarco, P., Espinosa, W. R., Guzewich, S. D., Levy, R. C., Miller, R. L., Chin, M., Kahn, R. A., Kemppinen, O., Moosmüller, H., Nowottnick, E. P., Rocha-Lima, A., Smith, M. D., Yorks, J. E., and Yu, H.: Mineral dust optical properties for remote sensing and global modeling: A review, Remote Sensing of Environment, 303, 113 982, https://doi.org/10.1016/j.rse.2023.113982, 2024.

https://doi.org/10.5194/egusphere-2024-3460
Preprint. Discussion started: 2 January 2025

Córdoba-Jabonero, C., Sicard, M., Ansmann, A., del Águila, A., and Baars, H.: Separation of the optical and mass features of particle components in different aerosol mixtures by using POLIPHON retrievals in synergy with continuous polarized Micro-Pulse Lidar (P-MPL) measurements, Atmospheric Measurement Techniques, 11, 4775–4795, https://doi.org/10.5194/amt-11-4775-2018, 2018.

Denjean, C., Cassola, F., Mazzino, A., Triquet, S., Chevaillier, S., Grand, N., Bourrianne, T., Momboisse, G., Sellegri, K., Schwarzenbock, A., Freney, E., Mallet, M., and Formenti, P.: Size distribution and optical properties of mineral dust aerosols transported in the western Mediterranean, Atmospheric Chemistry and Physics, 16, 1081–1104, https://doi.org/10.5194/acp-16-1081-2016, 2016.

Dieudonné, E., Chazette, P., Marnas, F., Totems, J., and Shang, X.: Lidar profiling of aerosol optical properties from Paris to Lake Baikal (Siberia), Atmospheric Chemistry and Physics, 15, 5007–5026, https://doi.org/10.5194/acp-15-5007-2015, 2015.

Ferrare, R., Hair, J., Hostetler, C., Shingler, T., Burton, S. P., Fenn, M., Clayton, M., Scarino, A. J., Harper, D., Seaman, S., Cook, A., Crosbie, E., Winstead, E., Ziemba, L., Thornhill, L., Robinson, C., Moore, R., Vaughan, M., Sorooshian, A., Schlosser, J. S., Liu, H., Zhang, B., Diskin, G., DiGangi, J., Nowak, J., Choi, Y., Zuidema, P., and Chellappan, S.: Airborne HSRL-2 measurements of elevated aerosol depolarization associated with non-spherical sea salt, Frontiers in Remote Sensing, 4, https://doi.org/10.3389/frsen.2023.1143944, 2023.

Filioglou, M., Giannakaki, E., Backman, J., Kesti, J., Hirsikko, A., Engelmann, R., O'Connor, E., Leskinen, J. T. T., Shang, X., Korhonen, H., Lihavainen, H., Romakkaniemi, S., and Komppula, M.: Optical and geometrical aerosol particle properties over the United Arab Emirates, Atmospheric Chemistry and Physics, 20, 8909–8922, https://doi.org/10.5194/acp-20-8909-2020, 2020.

Filioglou, M., Leskinen, A., Vakkari, V., O'Connor, E., Tuononen, M., Tuominen, P., Laukkanen, S., Toiviainen, L., Saarto, A., Shang, X., Tiitta, P., and Komppula, M.: Spectral dependence of birch and pine pollen optical properties using a synergy of lidar instruments, Atmospheric Chemistry and Physics, 23, 9009–9021, https://doi.org/10.5194/acp-23-9009-2023, 2023.

Freudenthaler, V., Esselborn, M., Wiegner, M., Heese, B., Tesche, M., Ansmann, A., Müller, D., Althausen, D., Wirth, M., Fix, A., Ehret, G., Knippertz, P., Toledano, C., Gasteiger, J., Garhammer, M., and Seefeldner, M.: Depolarization ratio profiling at several wavelengths in pure Saharan dust during SAMUM 2006, Tellus B: Chemical and Physical Meteorology, https://doi.org/10.1111/j.1600-0889.2008.00396.x, 2009.

Groß, S., Freudenthaler, V., Schepanski, K., Toledano, C., Schäfler, A., Ansmann, A., and Weinzierl, B.: Optical properties of long-range transported Saharan dust over Barbados as measured by dual-wavelength depolarization Raman lidar measurements, Atmospheric Chemistry and Physics, 15, 11 067–11 080, https://doi.org/10.5194/acp-15-11067-2015, 2015.

Groß, S., Tesche, M., Freudenthaler, V., Toledano, C., Wiegner, M., Ansmann, A., Althausen, D., and Seefeldner, M.: Characterization of Saharan dust, marine aerosols and mixtures of biomass-burning aerosols and dust by means of multi-wavelength depolarization and Raman lidar measurements during SAMUM 2, Tellus B: Chemical and Physical Meteorology, https://doi.org/10.1111/j.1600-0889.2011.00556.x, 2011.

Groß, S., Freudenthaler, V., Wiegner, M., Gasteiger, J., Geiß, A., and Schnell, F.: Dual-wavelength linear depolarization ratio of volcanic aerosols: Lidar measurements of the Eyjafjallajökull plume over Maisach, Germany, Atmospheric Environment, 48, 85–96, https://doi.org/10.1016/j.atmosenv.2011.06.017, 2012.

Haarig, M., Ansmann, A., Althausen, D., Klepel, A., Groß, S., Freudenthaler, V., Toledano, C., Mamouri, R.-E., Farrell, D. A., Prescod, D. A., Marinou, E., Burton, S. P., Gasteiger, J., Engelmann, R., and Baars, H.: Triple-wavelength depolarization-ratio profiling of Saharan dust over Barbados during SALTRACE in 2013 and 2014, Atmospheric Chemistry and Physics, 17, 10 767–10 794, https://doi.org/10.5194/acp-17-10767-2017, 2017a.

https://doi.org/10.5194/egusphere-2024-3460
Preprint. Discussion started: 2 January 2025

Haarig, M., Ansmann, A., Gasteiger, J., Kandler, K., Althausen, D., Baars, H., Radenz, M., and Farrell, D. A.: Dry versus wet marine particle optical properties: RH dependence of depolarization ratio, backscatter, and extinction from multiwavelength lidar measurements during SALTRACE, Atmospheric Chemistry and Physics, 17, 14 199–14 217, https://doi.org/10.5194/acp-17-14199-2017, 2017b.

Haarig, M., Ansmann, A., Baars, H., Jimenez, C., Veselovskii, I., Engelmann, R., and Althausen, D.: Depolarization and lidar ratios at 355, 532, and 1064 nm and microphysical properties of aged tropospheric and stratospheric Canadian wildfire smoke, Atmospheric Chemistry and Physics, 18, 11 847–11 861, https://doi.org/10.5194/acp-18-11847-2018, 2018.

Haarig, M., Walser, A., Ansmann, A., Dollner, M., Althausen, D., Sauer, D., Farrell, D., and Weinzierl, B.: Profiles of cloud condensation nuclei, dust mass concentration, and ice-nucleating-particle-relevant aerosol properties in the Saharan Air Layer over Barbados from polarization lidar and airborne in situ measurements, Atmospheric Chemistry and Physics, 19, 13 773–13 788, https://doi.org/10.5194/acp-19-13773-2019, 2019.

Haarig, M., Ansmann, A., Engelmann, R., Baars, H., Toledano, C., Torres, B., Althausen, D., Radenz, M., and Wandinger, U.: First triple-wavelength lidar observations of depolarization and extinction-to-backscatter ratios of Saharan dust, Atmospheric Chemistry and Physics, 22, 355–369, https://doi.org/10.5194/acp-22-355-2022, 2022.

Hofer, J., Althausen, D., Abdullaev, S. F., Makhmudov, A. N., Nazarov, B. I., Schettler, G., Engelmann, R., Baars, H., Fomba, K. W., Müller, K., Heinold, B., Kandler, K., and Ansmann, A.: Long-term profiling of mineral dust and pollution aerosol with multiwavelength polarization Raman lidar at the Central Asian site of Dushanbe, Tajikistan: case studies, Atmospheric Chemistry and Physics, 17, 14 559–14 577, https://doi.org/10.5194/acp-17-14559-2017, 2017.

Hofer, J., Ansmann, A., Althausen, D., Engelmann, R., Baars, H., Fomba, K. W., Wandinger, U., Abdullaev, S. F., and Makhmudov, A. N.: Optical properties of Central Asian aerosol relevant for spaceborne lidar applications and aerosol typing at 355 and 532 nm, Atmospheric Chemistry and Physics, 20, 9265–9280, https://doi.org/10.5194/acp-20-9265-2020, 2020.

Hu, Q.: Advanced aerosol characterization using sun/sky photometer and multi-wavelength Mie-Raman lidar measurements, Ph.D. thesis, Lille 1, www.theses.fr/2018LILUR078/document, 2018.

Hu, Q., Goloub, P., Veselovskii, I., Bravo-Aranda, J.-A., Popovici, I. E., Podvin, T., Haeffelin, M., Lopatin, A., Dubovik, O., Pietras, C., Huang, X., Torres, B., and Chen, C.: Long-range-transported Canadian smoke plumes in the lower stratosphere over northern France, Atmospheric Chemistry and Physics, 19, 1173–1193, https://doi.org/10.5194/acp-19-1173-2019, 2019.

Hu, Q., Wang, H., Goloub, P., Li, Z., Veselovskii, I., Podvin, T., Li, K., and Korenskiy, M.: The characterization of Taklamakan dust properties using a multiwavelength Raman polarization lidar in Kashi, China, Atmospheric Chemistry and Physics, 20, 13 817–13 834, https://doi.org/10.5194/acp-20-13817-2020, 2020.

Järvinen, E., Kemppinen, O., Nousiainen, T., Kociok, T., Möhler, O., Leisner, T., and Schnaiter, M.: Laboratory investigations of mineral dust near-backscattering depolarization ratios, Journal of Quantitative Spectroscopy and Radiative Transfer, 178, 192–208, https://doi.org/10.1016/j.jqsrt.2016.02.003, 2016.

Mahowald, N., Albani, S., Kok, J. F., Engelstaeder, S., Scanza, R., Ward, D. S., and Flanner, M. G.: The size distribution of desert dust aerosols and its impact on the Earth system, Aeolian Research, 15, 53–71, https://doi.org/10.1016/j.aeolia.2013.09.002, 2014.

Mallios, S. A., Daskalopoulou, V., and Amiridis, V.: Orientation of non spherical prolate dust particles moving vertically in the Earth's atmosphere, Journal of Aerosol Science, 151, 105 657, https://doi.org/10.1016/j.jaerosci.2020.105657, 2021.

Mamali, D., Marinou, E., Sciare, J., Pikridas, M., Kokkalis, P., Kottas, M., Binietoglou, I., Tsekeri, A., Keleshis, C., Engelmann, R., Baars, H., Ansmann, A., Amiridis, V., Russchenberg, H., and Biskos, G.: Vertical profiles of aerosol mass concentration derived by unmanned airborne in situ and remote sensing instruments during dust events, Atmospheric Measurement Techniques, 11, 2897–2910, https://doi.org/10.5194/amt-11-2897-2018, 2018.

Mamouri, R. E. and Ansmann, A.: Fine and coarse dust separation with polarization lidar, Atmospheric Measurement Techniques, 7, 3717–3735, https://doi.org/10.5194/amt-7-3717-2014, 2014.

Mamouri, R.-E. and Ansmann, A.: Potential of polarization lidar to provide profiles of CCN- and INP-relevant aerosol parameters, Atmospheric Chemistry and Physics, 16, 5905–5931, https://doi.org/10.5194/acp-16-5905-2016, 2016.

Mamouri, R.-E. and Ansmann, A.: Potential of polarization/Raman lidar to separate fine dust, coarse dust, maritime, and anthropogenic aerosol profiles, Atmospheric Measurement Techniques, 10, 3403–3427, https://doi.org/10.5194/amt-10-3403-2017, 2017.

Marenco, F. and Hogan, R. J.: Determining the contribution of volcanic ash and boundary layer aerosol in backscatter lidar returns: A three-component atmosphere approach, Journal of Geophysical Research: Atmospheres, 116, https://doi.org/10.1029/2010JD015415, 2011.

Marinou, E., Amiridis, V., Binietoglou, I., Tsikerdekis, A., Solomos, S., Proestakis, E., Konsta, D., Papagiannopoulos, N., Tsekeri, A., Vlastou, G., Zanis, P., Balis, D., Wandinger, U., and Ansmann, A.: Three-dimensional evolution of Saharan dust transport towards Europe based on a 9-year EARLINET-optimized CALIPSO dataset, Atmospheric Chemistry and Physics, 17, 5893–5919, https://doi.org/10.5194/acp-17-5893-2017, 2017.

Miffre, A., David, G., Thomas, B., Rairoux, P., Fjaeraa, A., Kristiansen, N., and Stohl, A.: Volcanic aerosol optical properties and phase partitioning behavior after long-range advection characterized by UV-Lidar measurements, Atmospheric Environment, 48, 76–84, https://doi.org/10.1016/j.atmosenv.2011.03.057, 2012.

Miffre, A., Cholleton, D., Noël, C., and Rairoux, P.: Investigating the dependence of mineral dust depolarization on complex refractive index and size with a laboratory polarimeter at 180.0° lidar backscattering angle, Atmospheric Measurement Techniques, 16, 403–417, https://doi.org/10.5194/amt-16-403-2023, 2023.

Murayama, T., Müller, D., Wada, K., Shimizu, A., Sekiguchi, M., and Tsukamoto, T.: Characterization of Asian dust and Siberian smoke with multi-wavelength Raman lidar over Tokyo, Japan in spring 2003, Geophysical Research Letters, 31, https://doi.org/10.1029/2004GL021105, 2004.

Nisantzi, A., Mamouri, R. E., Ansmann, A., and Hadjimitsis, D.: Injection of mineral dust into the free troposphere during fire events observed with polarization lidar at Limassol, Cyprus, Atmospheric Chemistry and Physics, 14, 12 155–12 165, https://doi.org/10.5194/acp-14-12155-2014, 2014.

Nishizawa, T., Okamoto, H., Sugimoto, N., Matsui, I., Shimizu, A., and Aoki, K.: An algorithm that retrieves aerosol properties from dual-wavelength polarized lidar measurements, Journal of Geophysical Research: Atmospheres, 112, https://doi.org/10.1029/2006JD007435, 2007.

Pappalardo, G., Amodeo, A., Apituley, A., Comeron, A., Freudenthaler, V., Linné, H., Ansmann, A., Bösenberg, J., D'Amico, G., Mattis, I., Mona, L., Wandinger, U., Amiridis, V., Alados-Arboledas, L., Nicolae, D., and Wiegner, M.: EARLINET: towards an advanced sustainable European aerosol lidar network, Atmospheric Measurement Techniques, 7, 2389–2409, https://doi.org/10.5194/amt-7-2389-2014, 2014.

Pearson, G., Davies, F., and Collier, C.: An Analysis of the Performance of the UFAM Pulsed Doppler Lidar for Observing the Boundary Layer, Journal of Atmospheric and Oceanic Technology, 26, 240–250, https://doi.org/10.1175/2008JTECHA1128.1, 2009.

Proestakis, E., Amiridis, V., Marinou, E., Georgoulias, A. K., Solomos, S., Kazadzis, S., Chimot, J., Che, H., Alexandri, G., Binietoglou, I., Daskalopoulou, V., Kourtidis, K. A., de Leeuw, G., and van der A, R. J.: Nine-year spatial and temporal evolution of desert dust aerosols over South and East Asia as revealed by CALIOP, Atmospheric Chemistry and Physics, 18, 1337–1362, https://doi.org/10.5194/acp-18-1337-2018, 2018.

https://doi.org/10.5194/egusphere-2024-3460
Preprint. Discussion started: 2 January 2025

Proestakis, E., Gkikas, A., Georgiou, T., Kampouri, A., Drakaki, E., Ryder, C. L., Marenco, F., Marinou, E., and Amiridis, V.: A near-global multiyear climate data record of the fine-mode and coarse-mode components of atmospheric pure dust, Atmospheric Measurement Techniques, 17, 3625–3667, https://doi.org/10.5194/amt-17-3625-2024, 2024.

Ryder, C. L., Marenco, F., Brooke, J. K., Estelles, V., Cotton, R., Formenti, P., McQuaid, J. B., Price, H. C., Liu, D., Ausset, P., Rosenberg, P. D., Taylor, J. W., Choularton, T., Bower, K., Coe, H., Gallagher, M., Crosier, J., Lloyd, G., Highwood, E. J., and Murray, B. J.: Coarse-mode mineral dust size distributions, composition and optical properties from AER-D aircraft measurements over the tropical eastern Atlantic, Atmospheric Chemistry and Physics, 18, 17 225–17 257, https://doi.org/10.5194/acp-18-17225-2018, 2018.

Ryder, C. L., Highwood, E. J., Walser, A., Seibert, P., Philipp, A., and Weinzierl, B.: Coarse and giant particles are ubiquitous in Saharan dust export regions and are radiatively significant over the Sahara, Atmospheric Chemistry and Physics, 19, 15 353–15 376, https://doi.org/10.5194/acp-19-15353-2019, 2019.

Sakai, T., Nagai, T., Zaizen, Y., and Mano, Y.: Backscattering linear depolarization ratio measurements of mineral, sea-salt, and ammonium sulfate particles simulated in a laboratory chamber, Applied Optics, 49, 4441–4449, https://doi.org/10.1364/AO.49.004441, 2010.

Shang, X., Giannakaki, E., Bohlmann, S., Filioglou, M., Saarto, A., Ruuskanen, A., Leskinen, A., Romakkaniemi, S., and Komppula, M.: Optical characterization of pure pollen types using a multi-wavelength Raman polarization lidar, Atmospheric Chemistry and Physics, 20, 15 323–15 339, https://doi.org/10.5194/acp-20-15323-2020, 2020.

Shang, X., Baars, H., Stachlewska, I. S., Mattis, I., and Komppula, M.: Pollen observations at four EARLINET stations during the ACTRIS-COVID-19 campaign, Atmospheric Chemistry and Physics, 22, 3931–3944, https://doi.org/10.5194/acp-22-3931-2022, 2022.

Shimizu, A., Sugimoto, N., Matsui, I., Arao, K., Uno, I., Murayama, T., Kagawa, N., Aoki, K., Uchiyama, A., and Yamazaki, A.: Continuous observations of Asian dust and other aerosols by polarization lidars in China and Japan during ACE-Asia, Journal of Geophysical Research: Atmospheres, 109, n/a–n/a, https://doi.org/10.1029/2002JD003253, d19S17, 2004.

Sugimoto, N. and Lee, C. H.: Characteristics of dust aerosols inferred from lidar depolarization measurements at two wavelengths, Applied Optics, 45, 7468–7474, https://doi.org/10.1364/AO.45.007468, 2006.

Szczepanik, D. M., Stachlewska, I. S., Tetoni, E., and Althausen, D.: Properties of Saharan Dust Versus Local Urban Dust—A Case Study, Earth and Space Science, 8, e2021EA001 816, https://doi.org/10.1029/2021EA001816, 2021.

Tesche, M., Ansmann, A., Müller, D., Althausen, D., Engelmann, R., Freudenthaler, V., and Groß, S.: Vertically resolved separation of dust and smoke over Cape Verde using multiwavelength Raman and polarization lidars during Saharan Mineral Dust Experiment 2008, Journal of Geophysical Research: Atmospheres, 114, https://doi.org/10.1029/2009JD011862, 2009.

Tesche, M., Müller, D., Gross, S., Ansmann, A., Althausen, D., Freudenthaler, V., Weinzierl, B., Veira, A., and Petzold, A.: Optical and microphysical properties of smoke over Cape Verde inferred from multiwavelength lidar measurements, Tellus B: Chemical and Physical Meteorology, https://doi.org/10.1111/j.1600-0889.2011.00549.x, 2011.

van der Does, M., Knippertz, P., Zschenderlein, P., Harrison, R. G., and Stuut, J.-B. W.: The mysterious long-range transport of giant mineral dust particles, Science Advances, 4, eaau2768, https://doi.org/10.1126/sciadv.aau2768, 2018.

Veselovskii, I., Goloub, P., Podvin, T., Bovchaliuk, V., Derimian, Y., Augustin, P., Fourmentin, M., Tanre, D., Korenskiy, M., Whiteman, D. N., Diallo, A., Ndiaye, T., Kolgotin, A., and Dubovik, O.: Retrieval of optical and physical properties of African dust from multi-wavelength Raman lidar measurements during the SHADOW campaign in Senegal, Atmospheric Chemistry and Physics, 16, 7013–7028, https://doi.org/10.5194/acp-16-7013-2016, 2016.

Welton, E. J., Campbell, J. R., Spinhirne, J. D., and III, V. S. S.: Global monitoring of clouds and aerosols using a network of micropulse lidar systems, in: Lidar Remote Sensing for Industry and Environment Monitoring, edited by Singh, U. N., Asai, K.,

https://doi.org/10.5194/egusphere-2024-3460
Preprint. Discussion started: 2 January 2025

Ogawa, T., Singh, U. N., Itabe, T., and Sugimoto, N., vol. 4153, pp. 151–158, International Society for Optics and Photonics, SPIE, https://doi.org/10.1117/12.417040, 2001.

Winker, D. M., Vaughan, M. A., Omar, A., Hu, Y., Powell, K. A., Liu, Z., Hunt, W. H., and Young, S. A.: Overview of the CALIPSO Mission and CALIOP Data Processing Algorithms, Journal of Atmospheric and Oceanic Technology, 26, 2310–2323, https://doi.org/10.1175/2009JTECHA1281.1, 2009.